Optimizing air distribution in floor and wall burners of an industrial steam cracking firebox: a CFD study

Florian Wéry[1], *Moreno Geerts*[1,2]

Laurien A. Vandewalle[1], *Pieter A. Reyniers*[2], *Geraldine J. Heynderickx*[1], *Guy B. Marin*[1], *Kevin M. Van Geem*[1]*

[1]Ghent University, Laboratory for Chemical Technology, Technologiepark 125, 9052 Ghent, Belgium.

[2]BASF Antwerpen, Scheldelaan 600, 2040 Antwerp, Belgium.

Author Contributions: The manuscript was written through contributions of all authors. All authors have given approval to the final version of the manuscript. ‡ Florian Wéry and Moreno Geerts contributed equally.

*Corresponding author: Technologiepark 125, 9052 Gent, Belgium; Kevin.VanGeem@UGent.be

Keywords: Computational Fluid Dynamics, steam cracking, NO_x emission

Abstract:

A 3D computational fluid dynamics model for an industrial scale steam cracking firebox is combined with a 1D reactor model for the cracking process within the reactor coil. This framework is validated using industrial tunable diode laser absorption spectroscopy (TDLAS) measurements in a naphtha steam cracking furnace. Industrial O_2, H_2O, CO and temperature data show good agreement with simulation results at different locations within the firebox. The influence of varying the primary-to-secondary air flow distribution to the floor and wall burners separately is investigated using the validated framework. Altering the primary-to-secondary air flow distribution of the floor burners from 75/25 to 25/75 results in a 66% increase in furnace run length and a 35% decrease in NO_x formation. This shift in air ratio ensures a lower rollover height of the flame and a large recirculation zone of the flue gas, spreading the radiative heat flux on the reactor coil more evenly. Altering the primary-to-secondary air flow distribution of the sidewall burners from 50/50 to 100/0 results in a 13% increase in run length and a 30% decrease in NO_x formation. More primary air towards the sidewall burners is found to lead to more evenly spread out flames along the wall, resulting in flame interactions between the different burners and a combined flow towards the center of the firebox. These interactions result in a more uniform tube metal temperature profile along the different passes of the coil.

1. Introduction

With an annual production of almost 300 million metric tons, ethene and propene are the crucial building blocks for specialized chemicals and plastics. As the global population and living standards rise, commodity chemical production is expected to increase [1-3]. Steam cracking of crude oil or shale gas remains the primary method for producing these chemicals, but sustainable alternatives like CO_2 or CH_4-derived pathways and electrification are being explored [1, 4-7]. To be competitive, these alternatives require significant feedstock price reductions and process improvements [8]. Additionally, transitioning to electrified steam cracking necessitates renewable energy sources, making traditional fossil feedstock cracking dominant in the foreseeable future [9].

A steam cracking unit is divided in a 'hot' section followed by a 'cold' section. The hot section includes the convection section where the feedstock is preheated, the radiant section with the reactor coil suspended in the firebox, and the transfer line exchanger (TLE) where the cracked gas stream is quenched. The cold section involves a separation train with distillation towers to isolate desired products from the cracked gas stream. This work focuses on the firebox, where floor and wall burners supply heat by burning methane-rich steam cracker off-gas.

Because of the significant heat requirements and the large scale at which steam cracking is performed, the process is responsible for around 8% of the global chemical industry's energy consumption making it the single most energy-consuming process in chemical industry, resulting in 260 Mt CO_2 emissions annually [10-13]. Considerable amounts of NO_x are also emitted which is more closely related to burner management on the fuel side of the firebox. Thermal NO_x production is generally dominant in steam cracking furnaces due to its exponential dependence on temperature and the absence of nitrogen containing compounds in the fuel [14-16]. So-called low-

NO_x burners are designed to achieve lower NO_x emissions by a variety of techniques with air staging being the most widely adopted [17]. This method increases the flame volume and subsequently reduces the peak flame temperature. Additionally, distinct regions with a fuel-lean or fuel-rich mixture can be achieved within a single burner to reduce NO_x emissions. Gas recirculation can also lower the peak flame temperature by reducing combustion rates. Post-processing techniques for the flue gas such as selective catalytic or non-catalytic reduction of NO_x can also be employed. Belal et al. recently experimentally investigated the effect of swirler burner design on exhaust emissions, concluding that low-swirl combustion is more efficient in reducing NO_x emissions compared to high swirl combustion [18]. Furthermore, different wall burner designs were recently investigated numerically by Herce et al. [19].

Steam cracking fireboxes are typically modeled via 0D or 1D models, but 3D computational fluid dynamics (CFD) models can more accurately capture the effect of the geometric design on operating conditions of a firebox. However, the computational cost associated with the use of 3D CFD is much higher than that for a 0D or 1D model. Recent CFD literature on steam cracking is predominantly focused on the reduction of both coke formation and CO_2 emissions [20-24]. The effect of different reactor coil designs on the coking rate was investigated by Dedeyne et al. [25]. A swirl flow tube reactor was investigated both experimentally and numerically by Schietekat et al. [26]. Vandewalle et al. performed dynamic computational fluid dynamics (CFD) simulations researching the impact of fouling on different reactor coil geometries [27]. As demonstrated both experimentally and numerically by Vangaever et al., the application of a high-emissivity coating to the refractory walls improves the energy efficiency and reduces the CO_2 emissions of the global steam cracking process [28, 29]. Rebordinos et al. studied different measures to increase energy efficiency in a steam cracking firebox [30]. A study in which both the firebox and reactor coils of an industrial firebox are modeled via CFD was recently performed by Rezaeimanesh et al. [31].

This study presents the first framework validated via tunable diode laser absorption spectroscopy (TDLAS) of an industrial steam cracking firebox. This framework combines a 3D CFD model at the fuel side with 1D reactor model equations on the process side. The developed framework is then used to determine optimal floor and wall burner operating conditions resulting in an increase of the furnace run length, i.e. the time between two decokes of the reactor coil, and a decrease of the NO_x emissions. In this regard, different primary-to-secondary air ratios towards the floor and wall burners are investigated.

2. MATHEMATICAL MODELS

2.1. *CONSERVATION EQUATIONS*

The firebox simulations presented here are performed using the commercial CFD software package Ansys® FLUENT 19.0, in line with previous work [22]. The conservation equations of mass, momentum and energy used in this work are given by Eq. (1) to (3):

$$\frac{\partial \rho}{\partial t} + \vec{\nabla} \cdot (\rho \vec{\mathrm{u}}) = 0 \tag{1}$$

$$\frac{\partial \rho \vec{u}}{\partial t} + \vec{\nabla} \cdot (\rho \vec{u} \vec{u}) = -\vec{\nabla} p + \vec{\nabla} \cdot \bar{\bar{\tau}} + \rho \vec{g} \tag{2}$$

$$\frac{\partial \rho H}{\partial t} + \vec{\nabla} \cdot (\rho H \vec{u}) = -\vec{\nabla} \cdot \vec{J}^H - \dot{q}_{rad} \tag{3}$$

The continuity and momentum equations are coupled via the Semi-Implicit Method for Pressure-Linked Equations (SIMPLE). The viscous stress tensor is given by Eq. (4):

$$\bar{\bar{\tau}} = (\mu + \mu_t) \left[\vec{\nabla} \vec{u} + \vec{\nabla} \vec{u}^T - \frac{2}{3} \left(\vec{\nabla} \cdot \vec{u} \right) \bar{\bar{I}} \right] \tag{4}$$

The enthalpy fluxes in the energy conservation equation are given by Eq. (5) based on Fourier's law of heat conduction

$$\vec{J}^H = -k\vec{\nabla}T = -\frac{k}{C_p}\vec{\nabla}H \tag{5}$$

Due to the compressible nature of the flow, Favre-averaged values, i.e. density weighted averages, instead of the standard Reynolds-averaged values, i.e. time weighted averages, are used to account for the turbulent flow behavior. Due to this averaging the Reynolds stresses appear in the momentum equations. In this work, the Re-Normalisation Group (RNG) k-ε model is used to close the momentum equations [32].

2.2. COMBUSTION MODEL

The GRI 3.0 kinetic network, comprising 53 species and 325 reactions, is used to model the non-premixed combustion in the steam cracking firebox [33]. In order to reduce the computational cost of calculating the net reaction rates for each species during each timestep of the 3D CFD simulation, non-adiabatic steady diffusion flamelet modeling is applied [34, 35]. This approach uses 1D counterflow diffusion flames for which exact solutions can be quickly calculated using specialized codes [36, 37]. Flamelet modeling approximates a turbulent flame by a wrinkled and distorted laminar flame, called a laminar flamelet. The adiabatic 1D diffusion flame is characterized by both the mixture fraction, Z, and the scalar dissipation rate, χ. A transport equation is solved for the flamelet mixture fraction, Z, and its variance, Z'. The mixture fraction has a value between 0 and 1: 0 for an oxidizer-only mixture and 1 for a fuel-only mixture. The balance equations for Z and Z' are given by Eq. (6) and (7) respectively:

$$\frac{\partial \rho Z}{\partial t} + \vec{\nabla} \cdot (\rho Z \vec{u}) = -\vec{\nabla} \cdot \vec{J}^Z \tag{6}$$

$$\frac{\partial \rho Z'}{\partial t} + \vec{\nabla} \cdot (\rho Z' \vec{u}) = \frac{\mu_t}{\sigma_t} \vec{\nabla} \cdot \left(\vec{\nabla} Z'\right) + c_g \mu_t \left(\vec{\nabla} \cdot Z'\right)^2 - c_x \rho \frac{\varepsilon}{k} {Z'}^2 \tag{7}$$

Herein, σ_t, c_g and c_x are model constants with a value of 0.85, 2.86 and 2.0 respectively [38]. The species flux $\vec{J}^Z$ is modeled using Fick's law for species diffusion, as depicted in Eq. (8):

$$\vec{J}^Z = \rho D_Z \vec{\nabla} Z \tag{8}$$

The scalar dissipation rate is a measure for the straining of the flame, which for a 1D flame increases by increasing the velocity of the fuel and oxidized jets or by decreasing the distance between the jets. It is calculated via Eq. (9).

$$\chi = 2 \frac{\tilde{\varepsilon}}{\tilde{k}} \widetilde{Z'^2} \tag{9}$$

When the scalar dissipation rate has a value close to 0, the combustion chemistry tends to equilibrium, whereas local quenching occurs when this value increases. When radiation is the predominant means of heat transfer, an extra variable that accounts for the non-adiabatic CFD cells, the enthalpy defect, needs to be introduced [39]. The enthalpy defect, ξ, is a measure for the distance from thermodynamic equilibrium within the cell. It is defined as the difference between the enthalpy of the calculated adiabatic flame, h, and the enthalpy of the fuel and oxidizer in a CFD cell, given by Eq. (10):

$$\xi = h - \left[h_0 + Z\left(h_f - h_0\right)\right] \tag{10}$$

with h_0 and h_f the enthalpy of oxidizer and fuel respectively. This defect is mainly caused by radiation in the internal and boundary CFD cells and convective heat transfer at the boundary CFD cells.

The formation of thermal NO_x proceeds kinetically much slower than the fuel gas oxidation reactions leading to inaccurate NO_x concentrations when determined via flamelet modeling.

Therefore, thermal NO_x formation in this work is modeled using the well-validated Zeldovich mechanism within FLUENT [14].

In this work, a lookup table is generated in a pre-processing step. This table contains flamelet information on mixture fraction, its variance and enthalpy defect to be used in the CFD simulation to help decrease the computational cost. Resulting species concentrations and temperature are then obtained via lookup in this table during calculations.

2.3. *Radiation modeling*

At the temperatures required to induce the endothermic cracking reactions, heat transfer is dominated by radiation. In this work, the Discrete Ordinates Model (DOM) is used to solve for radiative heat transfer [40, 41]. The model uses and solves the radiative transfer equation (RTE), given by Eq. (11) assuming the influence of scattering is negligible. In this work, each octant of the 3D space is discretized in 2 by 2 angular intervals.

$$\hat{s} \cdot \vec{\nabla} I_\lambda(r, \hat{s}) + \kappa_\lambda I_\lambda(r, \hat{s}) = \kappa_\lambda I_{b\lambda} \tag{11}$$

Herein, $I_\lambda(r, \hat{s})$ represents the spectral intensity of wavelength λ at location r in direction $\hat{s}$, κ_λ denotes the spectral absorption coefficient and $I_{b\lambda}$ is the spectral black body intensity at wavelength λ. The first term on the left hand side of Eq. (11) models the radiative intensity change along the direction $\hat{s}$. Absorption along the direction $\hat{s}$ is accounted for via the second term while the term on the right hand side accounts for the increase of the intensity change due to emission.

The weighted sum of gray gas model (WSGGM), developed by Smith, is used to reduce the number of times the RTE needs to be evaluated [42]. The most important species that absorb and emit radiation in combustion applications are CO_2 and H_2O. The WSGGM incorporates one clear band to simulate the so-called transparent regions in the electro-magnetic spectrum where no radiation is absorbed or emitted by the CO_2 and H_2O molecules. In the WSGGM, a non-gray gas is approximated by N fictional gray gases, which all have a specific constant absorption coefficient κ_i and a temperature dependent weight factor a_i. The non-gray gas emissivity over a path length L is then calculated by Eq. (12) for each fictional gray gas.

$$\varepsilon = \sum_{i=1}^{4} a_i(T)(1 - e^{-\kappa_i L}) \tag{12}$$

In all calculations presented here, a WSGGM consisting of four bands utilizing the model parameters by Smith et al. is employed [42].

2.4. *Reactor coil modeling*

Performing reactive 3D CFD simulations of a full steam cracking reactor coil while solving a coupled ordinary differential equation (ODE) for each individual species is not feasible due to the related excessive computational cost. However, given the high Reynolds numbers inside the reactor coils, radial gradients of variables can be neglected. Consequently the assumption of 1D plug flow can be made [43, 44] and COILSIM1D®, a steam cracking simulation package, can be applied in this work [45]. COILSIM1D® combines a single-event micro-kinetic model with 1D reactor equations, allowing to perform reactor simulations within seconds while considering a large number of species. The kinetic model implemented in COILSIM1D® comprises 750 species and thousands of elementary reactions [43, 45]. The reaction rate coefficients are calculated using a group contribution method developed by Sabbe et al. [46]. For each reaction family, a reference reaction is defined. This reference reaction is used as a basis on which perturbation terms are added depending on the specific structure of the considered species in the reaction. Rate coefficients for elementary steps are determined by adding corrections to the reference values based on group additive values, which depend on structural differences between the considered reaction and the reference reaction [47]. This method also corrects the pre-exponential factors for possible tunneling and hinderance due to rotation.

Due to the non-isothermal, non-adiabatic and non-isobaric nature of steam cracking, the reactor model consists of conservation equations for mass, momentum and energy, shown in Eqs. (13) to (15) respectively:

$$\frac{dF_i}{dz} = R_i A \tag{13}$$

$$\sum_i F_i \cdot C_{p,m,i} \cdot \frac{dT}{dz} = \omega\dot{\mathrm{q}} + \mathrm{A}\left(\sum_i R_i h_i\right) \tag{14}$$

$$-\frac{dp_t}{dz} = \left(\frac{2f}{d_t} + \frac{\varsigma}{\pi r_b}\right)\rho_g u^2 + \rho_g u \frac{du}{dz} \tag{15}$$

The run length of a steam cracking firebox is primarily determined by coke formation, characterized by the tube metal temperature (TMT) and pressure drop over the reactor coils. In order to determine the run length of the simulated firebox, a coking rate model is developed based on the pressure drop evolution of an industrial naphtha cracker. The pressure drop evolution over several run lengths of the firebox is normalized and corrected for process upsets and changes in operating conditions. The coking model of Reyniers, $r_{c,ref}$, is used as starting point [48]. This coking rate model is adapted to incorporate the decreasing heterogeneous catalytic coke formation according to Eq. (16).

$$r_{c,corr} = \left(C_1\, e^{\frac{-\mathrm{t}}{C_2}} + C_3\right) r_{c,ref} \tag{16}$$

Herein, C_1, C_2 and C_3 are parameters which are fitted to obtain an identical pressure drop increase curve in the simulations compared to the one obtained using the industrial data. The finally obtained coking rate correction factors are implemented in COILSIM1D® and are used to calculate the coke buildup and run lengths. The coking rate is assumed to remain constant during an entire

COILSIM1D® timestep. The timestep imposed in the run length simulations is 24 hours, in line with previous work [27]. The growing coke layer increases the heat transfer resistances between the flue gases and the process gas. To achieve an identical cracking severity at the outlet of the coil during the whole run length, the original incident radiative heat flux (IRHF) profile obtained from the start-of-run 3D CFD simulations is scaled which in turn increases the TMTs. After updating both the IRHF and TMT profile, a new COILSIM1D® simulation is started. This iterative procedure is continued until end-of-run conditions are reached. In this work, a maximum allowable TMT of 1350 K is set as the stopping criterion.

The TLE model used in this work accounts for additional reaction during the cooling of the process gas. The one-dimensional conservation equations for species, momentum, and energy as described in this section are used to simulate the process side of the TLE. The mass flow on the water-steam sides is determined by buoyancy and natural convection. The boundary condition on the water-steam side is set to a fixed temperature, corresponding to the saturation temperature of water at the considered pressure of 120 bar.

2.5. *FIREBOX - REACTOR COIL COUPLING*

The 3D firebox-1D reactor coil coupling used in this work is an optimized version of the coupling scheme developed by Plehiers et al. [49]. In this work, the CFD firebox simulation using Ansys® FLUENT is initialized using initial guesses for process gas temperatures and overall heat transfer coefficients, obtained by preliminary 1D reactor coil simulations within COILSIM1D®. The firebox is simulated iteratively until the bridge wall temperature, i.e. the area-averaged flue gas temperature at the outlet of the firebox, changes less than 1 K over 1000 subsequent iterations in the CFD framework. Next, the circumferentially averaged net heat flux over the reactor coil is extracted from the 3D firebox simulation results and imposed on the 1D reactor coil using

COILSIM1D®. The 1D reactor coil simulation provides process gas temperature and global heat transfer coefficient profiles, which are in turn imposed in the firebox simulation. This iterative coupling process is continued until the maximum change in process gas temperature between iterations is less than 0.5 K for all axial reactor coil coordinates.

Using the process gas temperature and corresponding global heat transfer coefficient profiles from the 1D reactor simulation in the 3D CFD simulation results in the possibility to see differences in TMT along the circumference of the reactor coils. This is important to be able to verify radiation shielding effects in steam cracking fireboxes. Additionally, this coupling approach results in a reduced number of firebox-reactor coil iterations, typically between 2 and 5.

3. TUNABLE DIODE LASER ABSORPTION SPECTROSCOPY SET-UP

Tunable diode laser absorption (TDLAS) measurements is used to measure species concentrations and temperature along a laser path. In this work, O_2, H_2O and CO concentrations are analyzed in an industrial steam cracking firebox.

A diode laser signal is absorbed partially by the species being examined. The non-absorbed part of the signal is caught by a receiver at the other end of its path. By tuning the laser to frequencies in which only the species of interest has strong absorbing bands, the extent of absorption by this species can be determined. This extent of absorption is then used to calculate the average concentration of the selected species along the laser trajectory through the firebox via the Beer-Lambert law, shown in Eq. (17).

$$I(\lambda) = I_0(\lambda)e^{-\alpha(\lambda)\,L} = I_0(\lambda)e^{-\sigma(\lambda)\,N_x\,L} = I_0(\lambda)e^{-\sigma(\lambda)\,N_A\,C_x\,L} \tag{17}$$

Herein, $I(\lambda)$ represents the radiation intensity after passing through the measured medium over a length L, $\alpha(\lambda)$ the absorbance of the medium and $\sigma(\lambda)$ the absorption cross-section, dependent on the wavelength. N_x, N_A and C_x represent the number density of the absorbing molecules, the Avogadro constant and the molar concentration of molecule x respectively.

The temperature is obtained based on the absorption by H_2O in two different bands via a method similar as the one described by So et al. [50]. The absorption in one band increases with increasing temperature while the absorption in the other band decreases. Consequently, the absorption ratio for the two bands can be used as a measure for the average temperature over the path length L.

A central control rack is used to guide the laser signal to several different sending heads. This rack contains the laser generation and optical fiber cables that are used to guide the photons of the laser beam to the sending heads. The laser is sent to each head one by one in a loop. This implies that for each path a new measurement can be taken every 5 minutes, which is sufficient to see the effect of changing parameters in a large, slowly changing system such as a steam cracking firebox.

An important aspect to consider when evaluating the TDLAS measurements results is the effect of the measurement geometry on those results. A schematic representation of the measurement device is given in the upper region of Figure 1. As can be seen, the sending and receiving heads are located outside the firebox. The laser thus not only measures the combustion gases within the firebox, but also the gases in the tube through the furnace wall. Those gases are at a significantly lower temperature due to the insulation of the furnace walls and the cooling by the ambient air. As a result, the temperature output of the measurement device is lower than the actual average flue gas temperature across the measurement line in the firebox. Additionally, the composition of the flue gas in the sighting tube closely resembles the composition of the flue gas near the firebox end wall, resulting in the composition near the firebox wall to be measured over a longer path. Therefore, a proportionally larger weight is given to the near-wall flue gas composition in the measurement value.

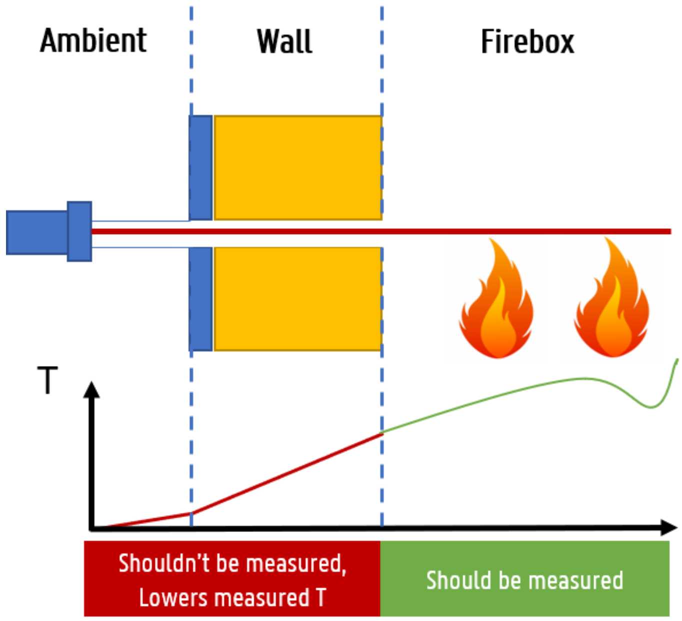

Figure 1: Schematic representation of the measurement set-up (top) highlighting the zones outside the firebox where temperature drops (bottom). The laser head is located outside of the firebox (left)

4. Geometry and simulation set-up

The geometry of the reactor coil is shown in Figure 2. It consists of eight inlets entering the furnace at the top near the end walls, four at each side end wall. Due to symmetry at the center, only half of the firebox needs to be simulated. The coils have three bends and make four passes through the firebox before combining two-by-two near the top of the firebox to four larger diameter coils. These four larger diameter coils have another two bends and passes before combining in a tetra-fitting at the center of the firebox roof. The combined process gas is sent to a single transfer-line exchanger (TLE) outside of the firebox to cool the process gas and inhibit further cracking reactions.

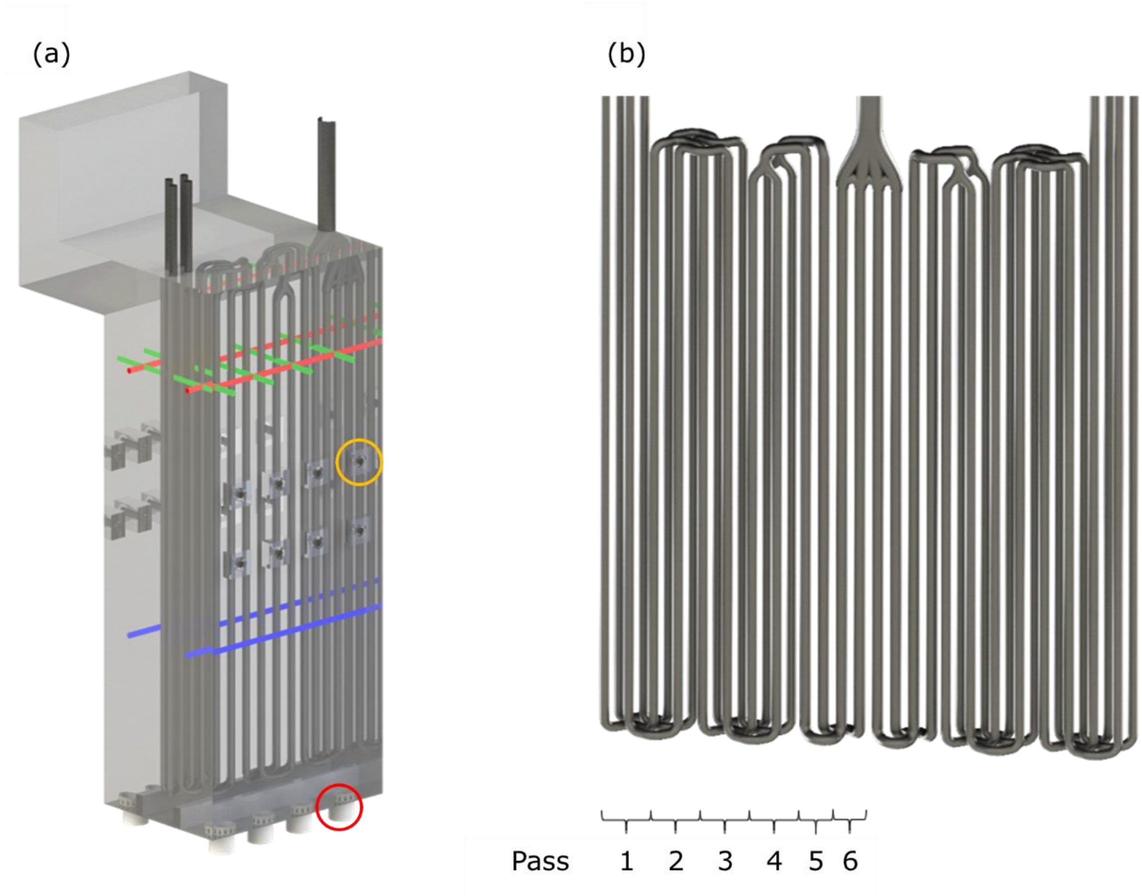

Figure 2: Schematic of the furnace section (half of the firebox) including the TDLAS measuring paths indicated in different colors: lower long paths in blue, upper long paths in red and upper short paths in green (a) and the full reactor geometry (b). A wall and floor burner are encircled in orange and red respectively.

A total of 16 non-premixed floor burners and 32 partially premixed wall burners are present in the full firebox, providing heat to the reactor. Due to confidentiality agreements between the industrial partner and the burner supplier, only a general description of the burner design of both the floor and wall burners is given. Both the floor and wall burners are equipped with staged oxygen injection. On both the floor and wall burners, the ratio of primary and secondary air flow can be tuned. This secondary air reaches the flame only after the combustion reaction has been initiated sub-stoichiometrically by the primary air. For the wall burners, the primary air enters the firebox premixed with the fuel.

A total of 12 pairs of sending and receiving head are used for TDLAS measurements to be able to pinpoint problematic areas in the firebox, as indicated on Figure 2a. Eight of the laser paths, indicated in green, are located across the short side of the firebox. Since Figure 2a shows half the full reactor coil, only four are drawn. On the same height, two long paths are present, indicated in red. These ten paths result in a grid located above the sidewall burners to achieve sufficient spatial resolution when gathering measurement values. Another two long paths, indicated in blue, are located below the sidewall burners that allow to discriminate between issues resulting from a floor or wall burner.

All relevant geometric details and process conditions used in the simulations at start-of-run are listed up in Table 1. A detailed PIONA analysis of the naphtha feedstock is provided in Table 2.

The geometry shown in Figure 2a is discretized into 19.2 million cells making use of both OpenFOAM's cell snapping tool *snappyHexMesh* and the adaptive mesh refining capabilities within FLUENT. As the furnace geometry comprises a wide range of spatial dimension, strong local grid refinement is required to solve the small burner tips, while a coarser grid can be used for the upper firebox parts. Grid refinements are thus mostly made near the fuel tips of both the floor and wall burners. This was achieved through the use of stepwise octree refinement. The level of refinement is identical to the refinement used in previous work [22].

Table 1: Firebox geometric features and operating conditions

Simulated firebox dimensions	
Length (m)	3.955
Width (m)	2.8
Height (m)	9.912
Firing conditions	
Fuel flow rate per floor burner (kg/s)	0.026
Air flow rate per floor burner (kg/s)	0.48
Air equivalence ratio floor burner	0.9
Fuel flow rate per wall burner (kg/s)	0.0075

Air flow rate per wall burner (kg/s)	0.133
Air equivalence ratio floor burner	0.9
Fuel/air inlet temperature (K)	300
Firebox outlet pressure (Pa g)	-132
Fuel composition	
CH_4 (wt%)	96.7
H_2 (wt%)	2.5
C_2H_4 (wt%)	0.8
Operating conditions	
Steam dilution (kg_{H2O}/kg_{HC})	0.4
Crossover temperature (K)	898
Coil outlet pressure (Pa)	297 000
Severity index: $C_{3=}/C_{2=}$	0.705
Material properties	
Firebox refractory emissivity	0.5
Coil tube skin emissivity	0.9
Reactor coil dimensions	
Number of inlet passes	4
Number of outlet passes	2
Wall thickness (m)	0.00675

Table 2: Detailed PIONA analysis of the naphtha feedstock

	n-Paraffins (wt%)	i-Paraffins (wt%)	Olefins (wt%)	Naphthenes (wt%)	Aromatics (wt%)
C_4	2.03	0.38	0.00	0.00	0.00
C_5	10.94	7.32	0.00	1.08	0.00
C_6	10.00	10.79	0.00	6.53	1.38
C_7	5.17	9.98	0.00	11.35	1.52
C_8	2.75	3.38	0.00	4.02	1.60
C_9	1.57	2.70	0.00	2.21	1.22
C_{10}	0.57	1.49	0.00	0.00	0.00

5. Results and discussion

5.1. *Validation study*

Making use of the TDLAS measurements, a thorough CFD validation is performed against data obtained from the four long laser paths. The signal along the short paths can vary significantly if a single burner is not operating as desired in the industrial plant, resulting in a large spread of the signals over time. It often happens that one or more burners do not operate properly, resulting in the need for the operator to adjust the air flow to these burners or to have them cleaned. The short path measurements are therefore interesting for the optimization of the furnace operation, but less interesting for CFD validation. Next to this, the long path measurements are more accurate due to their longer absorption paths, resulting in an increase of the total absorption and the signal-to-noise ratio. Additionally, the influence of wall effects on measured values is reduced due to the longer path. For the short and long paths, the length of the wall and ambient region depicted in Figure 1, corresponds to 36% and 15% of the path length respectively. Different ratios of primary-to-secondary air flowrates have been examined to closely match the industrial data. Averaged TDLAS measurements are used for validation since it is impossible to accurately measure the air flowrates to all air entrances of a burner and impose these in the simulation. The best agreement is found for a primary-to-secondary air flowrate of 45/55 for the floor burners and 50/50 for the sidewall burners. Herein, X/Y refers to X% of the total air going to the primary air duct and Y% going to the secondary air duct.

The industrially measured values and simulation values are gathered in Table 3, together with the averaged standard deviation. This averaged standard deviation is calculated by taking the average of the standard deviations of all measurements separately. The industrial data are measurements averaged over the first five days of three different naphtha steam cracking runs. The first five days were selected to obtain the best possible values for start-of-run conditions. When comparing the differences between the simulation and measurement results, an overall good agreement can be found, especially for the temperature and O_2 concentration. The underestimation of the H_2O content in the flue gas stems from the assumption dry air is supplied to the firebox. A significant difference of around 23% is observed for the CO concentration, which could both be a modeling and a measurement error. Generally, providing more oxygen to a flame reduces the CO content, which is confirmed in the simulations, but not in the plant data. The CO concentration can also be overpredicted for the upper path because of the flamelet approach, as mentioned before in literature [34, 51]. As H_2O and CO_2 are the most important species to be modeled because of their radiative properties, the deviation on the CO modeling is deemed acceptable as the other furnace measurements and simulation data agree very well.

Table 3: TDLAS measurement data of a naphtha steam cracking reactor compared to simulation data with operating conditions given in Table 1.

	Measurement		**St. dev.**	**Simulation**		**Rel. dev. (%)**	
Path	**Lower**	**Upper**		**Lower**	**Upper**	**Lower**	**Upper**
T (K)	1468	1391	15	1481	1357	+ 0.9	- 2.4
O_2 (vol%)	0.83	0.60	0.15	0.86	0.62	+ 3.6	+ 3.3
H_2O (vol%)	19.39	20.26	0.4	18.7	18.9	-3.6	-6.7
CO (vol%)	1.14	0.82	0.15	0.88	1.01	- 22.8	+ 23.2

Next to TDLAS measurements, other plant data such as the coil outlet temperature (COT) and propene-to-ethene ratio (P/E) are reported. The P/E ratio is a measure for the obtained cracking severity, with lower values implying a higher severity. A comparison between the plant data and the simulated values is made in Table 4. The P/E is found to be the variable that is most sensitive to operational changes. It can thus be considered the most reliable variable for validation purposes. The excellent agreement between simulated and plant P/E after the TLE as well as the COT is a strong indication of a correct simulation framework.

The TMT is measured using a handheld pyrometer. It is tremendously hard to locate and measure the hottest spot on the reactor coil. Still, a good agreement between simulations and plant data is obtained. A difference of 40 K, or 2.09%, is observed between the simulated and measured bridgewall temperature (BWT). Additionally, there is a discrepancy between the simulated bridgewall O_2 and measured stack O_2 concentration. There is no bridgewall O_2 measurement available in the plant data, but this discrepancy is a generally known issue in older steam cracking fireboxes. Near and beyond the bridgewall, additional cold air gets sucked into the furnace via unintentional openings, causing the stack O_2 concentration to be higher than the one at the bridgewall. Since the TDLAS O_2 measurements agree well with the simulated values, the air supply via the burners is assumed to be correct. Possibly there is a significant amount of cold air ingress via the coil inlet openings in the firebox roof or via other holes around the bridgewall. This results in a decrease in BWT as measured by the thermocouple due to the cold air entrained by the flue gas.

Table 4: Comparison between industrial data and the obtained simulated data with operating conditions specified in Table 1. The validating measurements are indicated in bold.

	Measurement	Simulation	Rel. dev. (%)
CIT (K)	853	853	-
BWT (K)	**1437**	**1477**	**+ 2.09**
COT (K)	**1059**	**1056**	**- 0.28**
P/E after coil	/	0.713	-
P/E after TLE	**0.71**	**0.711**	**± 0.14**
Maximal TMT (K)	**1253**	**1266**	**+ 1.04**
O_2 BW (vol%)	/	0.85	-
O_2 stack (vol%)	1.7	/	-

5.2. Effects of air distribution

5.2.1. Floor burners

Simulations using different primary-to-secondary air ratios for the floor burners are performed to investigate the effect of these changing operating conditions on the furnace performance. Herein, the effect on flame shape, TMTs, run length and NO_x formation is assessed. To compare, two simulations with air ratios of 25/75 and 75/25 are employed for the floor burners while a fixed ratio of 50/50 is set for the wall burners.

Figure 4 displays streamlines of air coming from the floor burners, colored by temperature. When comparing the streamlines for the 2 ratios, a large recirculation zone in the middle of the furnace is observed when using more secondary air (25/75, Figure 4b). This can be explained by a reduced upward momentum. Air coming from the primary air inlet only has a vertical velocity component which gets swirled, while the secondary air inlets enter the furnace under an angle radially outward of the burner. The primary air gains additional upward momentum due to the entrainment created by the fuel that exits the fuel nozzle at a significantly higher velocity than the primary air leaves its corresponding nozzle. The increased horizontal momentum in the 25/75 case results in merging of the flames and a lower rollover height of the flame. As the burner spacing between the two burners in the center of the furnace is larger than between any two other burners, the recirculation occurs there. Additionally, the interaction between the floor and sidewall burners changes due to this recirculation zone. In the 75/25 case the flue gases generated by the sidewall burners only go up. In the 25/75 case the flue gases also go down into the recirculation zone, resulting in a further increase of the recirculation volume.

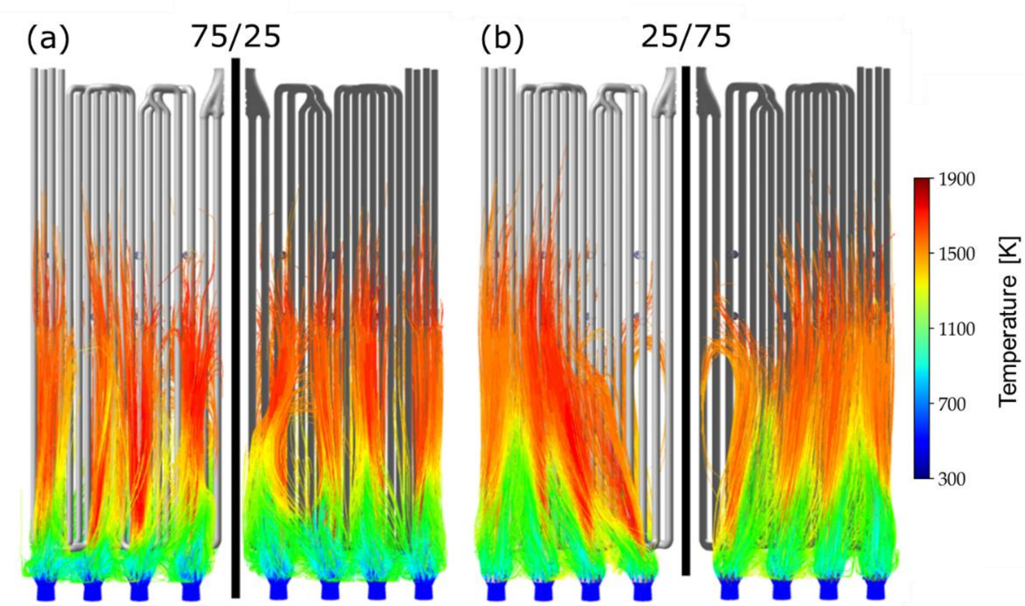

Figure 4: Air streamlines colored by temperature using primary-to-secondary air ratios on floor burners of 75/25 (a) and 25/75 (b). The black line indicates the axis of symmetry.

To further examine the effect of the flames, the IRHF over the simulated coils in the 75/25 case and the 25/75 case is displayed in Figure 5. It can be seen that the spread in IRHF on the first four passes is significantly larger in the 25/75 case (Figure 5b) compared to the 75/25 case (Figure 5a), especially in the lower regions of the furnace. The larger spread is a result of the non-parallel flow pattern of the flames and the corresponding difference in radiative heat transfer in the 25/75 air configuration. However, when looking at the outlet IRHF in both cases (blue curves), the 25/75 case clearly has a lower IRHF peak compared to the 75/25 case. Additionally, the outlets in the 25/75 case have a more uniform IRHF over the furnace height, with the top and bottom of the furnace having a higher IRHF compared to the 75/25 case. This results in a lower maximum TMT in the 25/75 case as discussed next.

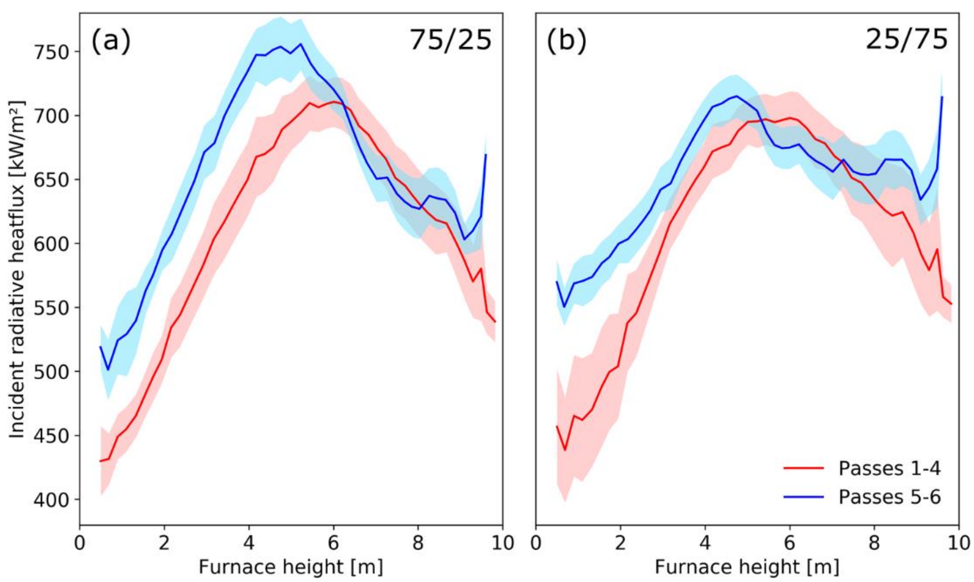

Figure 5: Circumferentially averaged IRHF for the different floor burner air ratio cases 75/25 (a) and 25/75 (b). IRHF on smaller diameter coils in passes 1-4 are indicated in red, larger diameter coils in passes 5 and 6 are indicated in blue. The IRHF has been averaged over the different passes. Passes 1-4 is the average of 16 IRHF profiles, Passes 5-6 is the average of 4 IRHF profiles. Standard deviations are indicated via an uncertainty band.

One of the most important operational limitations for steam cracking furnaces is the fact that a reactor alloy is bounded by a maximum allowable TMT. This maximum temperature should not be exceeded to avoid sudden integrity loss of a coil. When looking at the significantly different flame shapes and IRHF profiles, tube metal temperature profiles along the coil can be expected to vary considerably. Figure 6 displays the difference in tube metal temperatures between the 75/25 and the 25/75 case. The largest differences are located on the last three passes. Significantly lower TMTs are reached on the last three passes when more secondary air is fed to the burners (25/75 case).

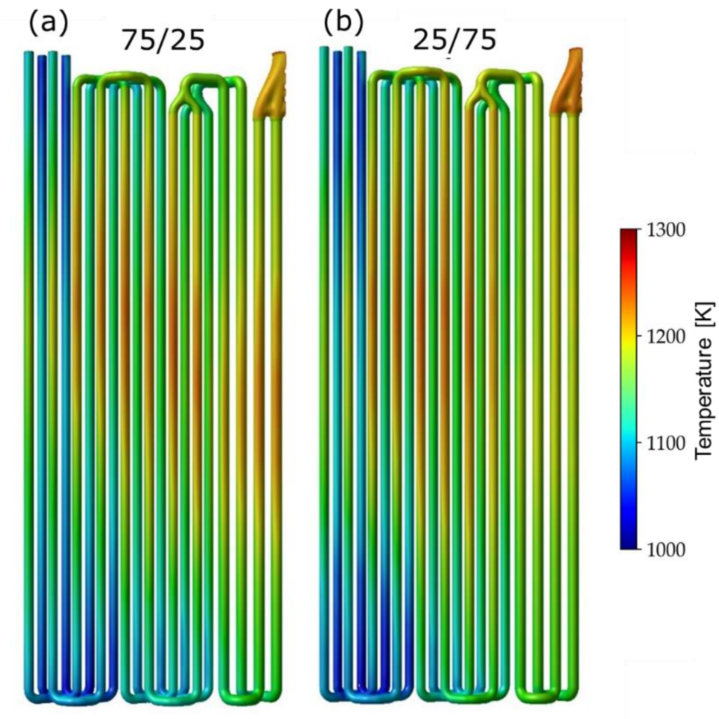

Figure 6: Tube metal temperatures with primary-to-secondary air ratios to the floor burners of 75/25(a) and 25/75(b)

To increase the run length of the furnace the effect of altering the process conditions on the TMT profile needs to be analyzed. Figure 7 displays the calculated circumferentially averaged TMT profile along the reactor coil axial coordinate at start-of-run (SOR) and end-of-run (EOR) conditions. TMT values increase with time due to coke formation on the tube internals. The presence of coke increases heat transfer resistance. This increase in heat transfer resistance in turn reduces the cracking severity within the coil. To maintain the latter, the IRHF is scaled as mentioned in section 2.5, resulting in increasing TMTs. The difference between TMT values at

EOR and SOR, as shown in Figure 7, increases with increasing tube length as the process gas temperature increases and more coke precursors are formed in the process gas near the tube outlet. When the TMT reaches 1350K the EOR condition is reached. The run length of the 25/75 case increases by 66% compared to the run length of the 75/25 case. The faster increase of coke formation and correspondingly TMT is explained by the higher IRHF peaks for the 75/25 case as shown in Figure 5. The more evenly distributed IRHF profile for the 25/75 results in a more even TMT profile, as seen in Figure 7, and thus a considerable increase in run length.

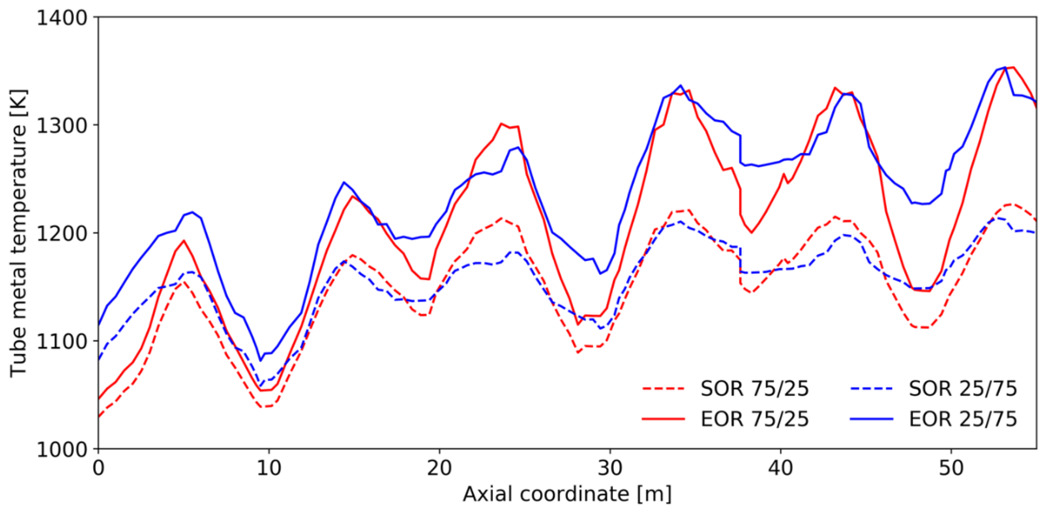

Figure 7: Circumferentially averaged tube metal temperatures along the reactor length at start-of-run and end-of-run using COILSIM1D®, with primary-to-secondary air ratios to the floor burners of 25/75 and 75/25

When analyzing the simulated NO_x concentrations at the exit of the firebox, a significant decrease is found when decreasing the amount of primary air. The 75/25 primary-to-secondary air ratio results in a calculated NO_x concentration of 590.9 mg/m³, compared to 385.8 mg/m³ for the 25/75 primary-to-secondary air ratio, which is a 34.7% decrease by adjusting the air registers to the burners.

The most indicating steam cracking process parameters are reported in Table 5 for both floor burner air flow distributions. The COT and P/E ratio are primarily related to the total amount of heat transferred to the steam cracking process gas. As discussed before, the maximum TMT value is higher in the 75/25 case compared to the 25/75. However, the total amount of heat transferred to the process gas is slightly higher for the 25/75 case under SOR conditions due to the more evenly distributed heat flux. This results in a slightly higher COT and slightly reduced P/E ratio, indicating more severe cracking of the naphtha. These same trends also hold under EOR conditions. Since the impact on the process gas remains rather limited, the primary impact of the burner operating regime lies in the heat distribution towards the reactor coil which impacts coking rates and furnace run length.

Table 5: Steam cracking coil conditions at SOR and EOR for the 75/25 and 25/75 floor burner air flow distributions

		75/25	25/75
SOR	COT (K)	1040.15	1042.46
	P/E after coil (-)	0.720	0.710
	TMT_{max} (K)	1226.68	1213.84
	Cumulative heat transfer (kW)	12844	13082
EOR	COT (K)	1041.47	1045.02
	P/E after coil (-)	0.720	0.709
	TMT_{max} (K)	1353.25	1353.25
	Cumulative heat transfer (kW)	12872	13118

5.2.2. Wall burners

To quantify the effect of a changing air distribution towards the sidewall burners, two different primary-to-secondary air flow rate ratios are imposed: 100/0 and 50/50. For the floor burners the ratio of 25/75 is maintained since this ratio gave rise to longer run length and lower NO_x formation, as discussed in the previous section. The 50/50 ratio is chosen as the limiting case due to industrial plant limitations. Secondary air can be introduced via a limited number of openings in the furnace wall around the sidewall burner. The flow is induced by the sub-atmospheric pressure present within the firebox and can be increased or decreased by changing the number of open ports. By opening all ports, up to 50% of the air needed for full combustion of the fuel flow to the sidewall burners can be entrained via the secondary air inlets.

As visualized in Figure 8, the 100/0 case results in spread out flames, covering the whole sidewall area due to the high velocity of the premixed fuel-air mixture exiting the burner head. In the 50/50 case on the other hand, more compact streamlines can be seen, resulting from the decreased radially outward momentum. A significant impact of the floor burner flow pattern and the corresponding recirculation zone for the 25/75 case as described in the previous section can be seen in the 50/50 case, i.e. the streamlines close to the symmetry plane are generally oriented downward due to the entrainment into the recirculation zone.

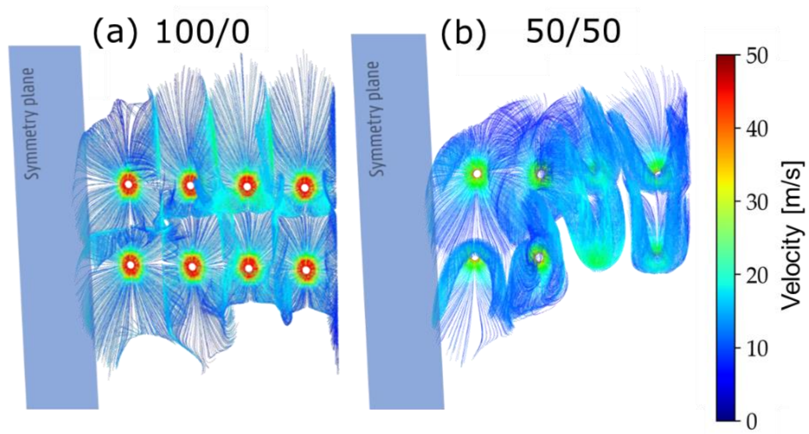

Figure 8: Air streamlines of wall burners for the 100/0 (a) and 50/50 (b) primary-to-secondary air ratios, colored by velocity

Figure 9 shows that the maximum TMTs achieved in the 100/0 case are higher than the ones in the 50/50 case, especially on passes 3 and 4. For the 100/0 case, two local maxima in TMT can be seen on each pass: one between the two rows of wall burners and one below the lower row of wall burners. This is an indication that the high velocities of the air leaving the sidewall burners in the 100/0 case result in interactions between both wall rows and between the bottom row and the floor burners. A combined flow occurs towards the center of the firebox. Therefore, increased TMTs are observed in these regions. This effect is not observed in the 50/50 case due to the limited radially outward velocity of the fuel-air mixture, resulting in a decreased interaction between the flue gases of the different burners.

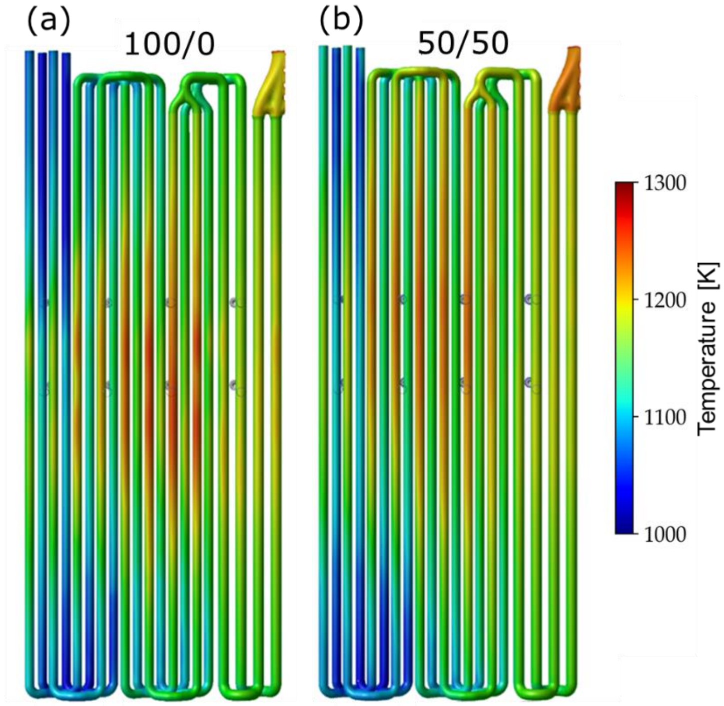

Figure 9: Tube metal temperatures with primary-to-secondary air ratios to the wall burners of 100/0 (a) and 50/50 (b), with floor burner primary-to-secondary air ratio of 25/75

The effect of the floor burner air distribution on the run length is smaller than that of the floor burners. A run length increase of 13% is observed for the 100/0 compared to the 50/50 case. Figure 10 displays the TMT profiles along the axial coordinate for the start-of-run and end-of-run conditions for both cases. It can clearly be seen that the TMTs on passes 3 and 4 are significantly higher for the 100/0 case as could also be observed in Figure 9. A slightly lower TMT can be seen at start-of-run on the 6th pass for the 100/0 case, which results in the extended run length compared to the 50/50 case. The maximum TMT at end-of-run conditions in the 100/0 case is observed at pass 4 and pass 6 simultaneously compared to only pass 6 in the 50/50 case. This means that there is a better heat distribution in the 100/0 case, causing the maximum TMT to be reached at multiple points simultaneously which prolongs the run.

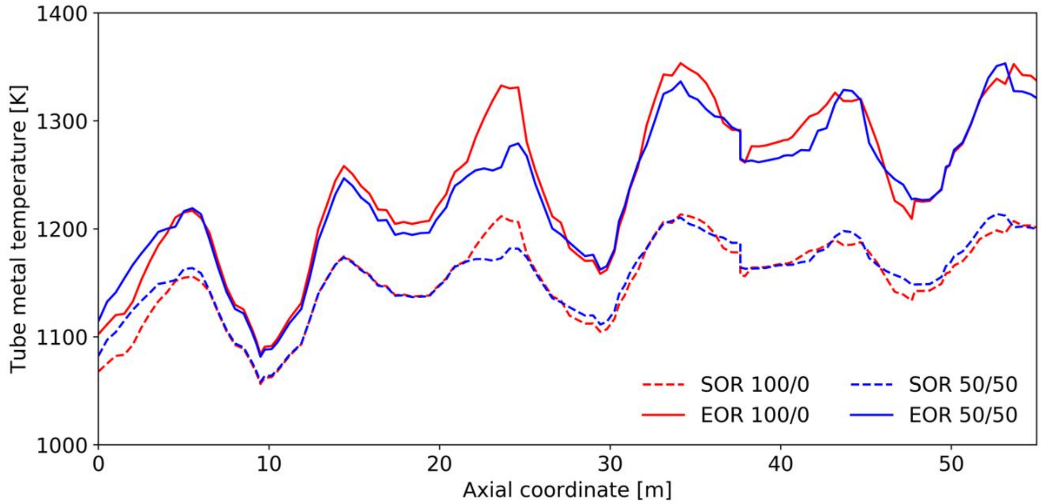

Figure 10: Circumferentially averaged tube metal temperatures along the reactor length at start-of-run and end-of-run using COILSIM1D®, with primary-to-secondary air ratios to the sidewall burners of 100/0 and 50/50 and floor burner primary-to-secondary air ratio fixed at 25/75

There is a decrease in NO_x formation with increasing primary air, i.e. 385.8 mg/m³ for the 50/50 case and 269.1 mg/m³ for the 100/0 case. This decrease is caused by the increased velocity of the fuel-air mixture exiting the wall burner head. An increased velocity results in a more spread-out flame. Although the peak temperature is higher in the 100/0 case, the residence time in this high temperature region is so low that a lower amount of NO_x is formed. Therefore, the shift to more primary air to the sidewall burners results in a reduction of NO_x formation.

In order to provide more insight in the formation of NO_x in the firebox, the NO_x mass fraction and temperature profiles at two cutting planes are shown in Figure 11 for a 50/50 air flow distribution in the wall burners. At the bottom of the firebox, the presence of the recirculation zone is clearly visible, shown by the deflection of the low NO_x-region at the rightmost floor burner. However, this is more pronounced at the front row of floor burners. While the NO_x concentration remains fairly low in the bottom part of the firebox, a drastic increase in NO_x concentration is visible at the height of the wall burners. Most NO_x is formed in this region due to the higher peak flame temperature associated with premixed burners. Close to stoichiometric combustion, premixed flames tend to form more NO_x compared to diffusion flames. Additionally, the flue gas velocity typically decreases along the furnace height, resulting in flue gas residing longer in this high temperature zone.

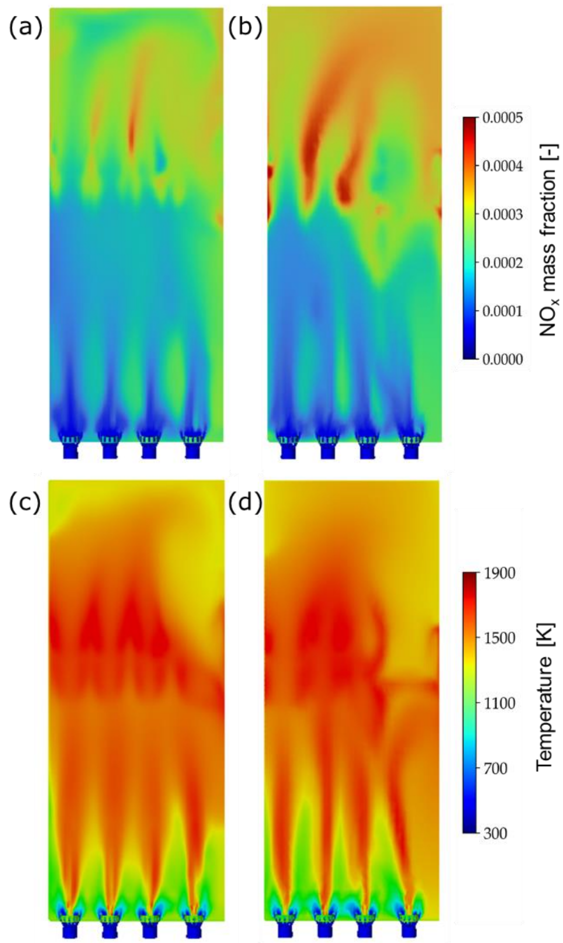

Figure 11: NO_x mass fraction (a, b) and temperature profiles (c, d) at two cutting planes of the firebox for a 50/50 wall burner air flow distribution. The cutting planes are located above the back row of floor burners in Figure 2a (a, c) and the front row of floor burner in Figure 2a (b, d)

For both wall burner air flow distributions, the most important steam cracking process parameters are reported in Table 6. Both under SOR and EOR conditions, the steam cracking parameters remain very close for both air flow distributions. This effect indicates that the air flow distribution towards the floor burners has a larger impact on the steam cracking process in this firebox geometry. At the bottom of the firebox, almost all heat supplied to the coil stems from the floor burners whereas the amount of heat transferred at the middle and top of the firebox is affected by both burner operating regimes. This combined effect can reduce the impact of the wall burner operating regime on the steam cracking process.

Table 6: Steam cracking coil conditions at SOR and EOR for the 100/0 and 50/50 floor burner air flow distributions

		100/0	50/50
SOR	COT (K)	1042.39	1042.46
	P/E after coil (-)	0.710	0.710
	TMT_{max} (K)	1213.46	1213.84
	Cumulative heat transfer (kW)	12954	13082
EOR	COT (K)	1045.86	1045.02
	P/E after coil (-)	0.709	0.709
	TMT_{max} (K)	1363.65	1353.25
	Cumulative heat transfer (kW)	13097	13118

6. CONCLUSIONS

A computational framework coupling Ansys® FLUENT with COILSIM1D® is set up to investigate the influence of individual burner adjustment to the performance of an industrial firebox for improving run length and reducing CO_2 and NO_x emissions. Tunable diode laser absorption spectroscopy measurements of an industrial firebox are, for the first time, used in validating the developed computational framework. Simulated O_2, H_2O, CO and temperature data showed good alignment with the industrial values.

The influence of the primary-to-secondary air ratio on the firebox performance is examined for both floor and wall burners. It is observed that switching from a primary-to-secondary air ratio of 75/25 to 25/75 in the floor burners greatly improves the performance of the firebox, resulting in an increase of 66% on the run length and a concurrent reduction of 35% in total NO_x formation.

For wall burners employing a 100/0 air flow distribution, higher local TMTs at start-of-run conditions are observed. However, this is accompanied with a more uniform heat transfer distribution. Also, higher flue gas velocities for the 100/0 distribution lead to a reduced residence time in the high-temperature region. These phenomena lead to a 13% increase in run length and 30% decrease in total NO_x emissions compared to the 50/50 air flow distribution.

The operational benefits of applying the air distribution strategies proposed in this work in industry can lead to an increase in feedstock flow rate, run length and coil outlet temperature at similar tube metal temperatures. This study shows that the primary-to-secondary air ratio indeed is influential on the firebox performance and should be considered in the operation of a steam cracking firebox. However, this analysis should be done on a per-cracker basis since the performance will depend on the type of coil and on the burner configuration.

NOMENCLATURE

ROMAN

a	Weight factor	$-$
A	Cross-sectional area	m^2
A	Pre-exponential factor	$-$
c	Model constant	$-$
C_p	Specific heat capacity	$J\ kg^{-1}K^{-1}$
$C_{p,m}$	Molar heat capacity	$J\ mol^{-1}K^{-1}$
d	Diameter	m
D	Diffusion coefficient	$m^2\ s^{-1}$
f	Fanning friction factor	$-$
F	Molar flow rate	$mol\ s^{-1}$
g	Gravitational constant	$m\ s^{-2}$
h	Molar enthalpy	$J\ mol^{-1}$
H	Specific enthalpy	$J\ kg^{-1}$
I_λ	Spectral intensity	$W\ sr^{-1}\ m^{-1}$
J^H	Enthalpy flux	$W\ m^{-1}$
J^Z	Mass flux	$kg\ m^{-2}\ s^{-1}$
k	Thermal conductivity	$W\ m^{-1}\ K^{-1}$
k	Turbulent kinetic energy	$m^2\ s^{-2}$
L	Length	m
p	Pressure	Pa
$\dot{q}$	Heat flux	$W\ m^{-2}$
r	Radius	m
r	Volumetric reaction rate	$mol\ m^{-3}\ s^{-1}$

R	Net production rate	$mol\,m^{-3}\,s^{-1}$
t	Time	s
T	Temperature	K
u	Velocity	$m\,s^{-1}$
w	Weight factor	$-$
z	Axial coordinate	m
Z	Mixture fraction	$-$

GREEK

ε	Turbulent dissipation rate	$m^2\,s^{-3}$
ε	Emissivity	$-$
ς	Nekrasov factor for tube bends	$-$
η	Efficiency	$-$
κ_λ	Spectral absorption coefficient	$-$
λ	Wavelength	m
μ	Dynamic viscosity	$Pa\,s$
ν	Stoichiometric coefficient	$-$
ξ	Enthalpy defect	$J\,mol^{-1}$
ρ	Density	$kg\,m^{-3}$
σ_t	Turbulent Prandtl number	$-$
$\bar{\bar{\tau}}$	Viscous stress tensor	$kg\,m^{-1}\,s^{-2}$
χ	Scalar dissipation rate	s^{-1}
ω	Circumference	m

SUB/SUPERSCRIPTS

b	Blackbody

c	Coking
f	Fuel
g	Gas
h	Enthalpy
i	Index/Species
o	Oxidizer
k	Coordinate
rad	Radial
t	Turbulent
Z	Mixture fraction
,	Variance
~	Favre-averaged value

ACRONYMS

BWT	Bridgewall temperature
CFD	Computational Fluid Dynamics
CIP	Coil inlet pressure
CIT	Coil inlet temperature
COT	Coil outlet temperature
DOM	Discrete ordinates model
EOR	End-of-run
IRHF	Incident radiative heat flux
ODE	Ordinary Differential Equation
P/E ratio	Propene-to-ethene ratio
SOR	Start-of-run
RNG	Re-Normalisation Group
RTE	Radiative transfer equation

SIMPLE	Semi-implicit method for pressure-linked equation
TLE	Transfer line exchanger
TMT	Tube metal temperatures
WSGGM	Weighted sum of gray gas models

ACKNOWLEDGMENTS

Florian Wéry and Moreno Geerts acknowledge financial support from a doctoral fellowship from the Fund for Scientific Research Flanders (FWO) under application number 1S97521N, 1248922N and by the Baekeland mandate HBC.2016.0594. The computational resources (Stevin Supercomputer Infrastructure) and services used in this work were provided by the VSC (Flemish Supercomputer Center), funded by Ghent University, FWO and the Flemish Government – department EWI. The research leading to these results has also received funding from the European Research Council (ERC) under the H2020 grant agreement no. 818607 (OPTIMA).

REFERENCES

[1] I. Amghizar, J. Dedeyne, D.J. Brown, G.B. Marin, K.M. Van Geem, Sustainable innovations in steam cracking: CO2 neutral olefin production, React. Chem. Eng. 5 (2020) 239-257. doi.org/10.1039/c9re00398c.

[2] Y. Gao, L. Neal, D. Ding, W. Wu, C. Baroi, A.M. Gaffney, F. Li, Recent Advances in Intensified Ethylene Production—A Review, ACS Catal. 9 (2019) 8592-8621. doi.org/10.1021/acscatal.9b02922.

[3] I. Amghizar, L.A. Vandewalle, K.M. Van Geem, G.B. Marin, New Trends in Olefin Production, Engineering 3 (2017) 171-178. doi.org/10.1016/J.ENG.2017.02.006.

[4] M. Yang, D. Fan, Y. Wei, P. Tian, Z. Liu, Recent Progress in Methanol-to-Olefins (MTO) Catalysts, Adv. Mater. 31 (2019) 1902181. doi.org/10.1002/adma.201902181.

[5] V. Zacharopoulou, A.A. Lemonidou, Olefins from Biomass Intermediates: A Review, Catalysts 8 (2018) 2. doi.org/10.3390/catal8010002.

[6] Y. Gambo, S. Adamu, R.A. Lucky, M.S. Ba-Shammakh, M.M. Hossain, Tandem catalysis: A sustainable alternative for direct hydrogenation of CO2 to light olefins, Appl. Catal., A 641 (2022) 118658. doi.org/10.1016/j.apcata.2022.118658.

[7] L. Berkelaar, J.v.d. Linde, J. Peper, A. Rajhans, D. Tiemessen, L.v.d. Ham, H.v.d. Berg, Electrochemical conversion of carbon dioxide to ethylene: Plant design, evaluation and prospects for the future, Chem. Eng. Res. Des. 182 (2022) 194-206. doi.org/10.1016/j.cherd.2022.03.034.

[8] Z. Zhao, J. Jiang, F. Wang, An economic analysis of twenty light olefin production pathways, J. Energy Chem. 56 (2021) 193-202. doi.org/10.1016/j.jechem.2020.04.021.

[9] K.M. Van Geem, V.V. Galvita, G.B. Marin, Making chemicals with electricity, Science 364 (2019) 734-735. doi.org/10.1126/science.aax5179.

[10] S.M. Sadrameli, Thermal/catalytic cracking of hydrocarbons for the production of olefins: A state-of-the-art review I: Thermal cracking review, Fuel 140 (2015) 102-115. doi.org/10.1016/j.fuel.2014.09.034.

[11] M.W.M. van Goethem, S. Barendregt, J. Grievink, P.J.T. Verheijen, M. Dente, E. Ranzi, A kinetic modelling study of ethane cracking for optimal ethylene yield, Chem. Eng. Res. Des. 91 (2013) 1106-1110. doi.org/10.1016/j.cherd.2013.01.006.

[12] T. Ren, M. Patel, K. Blok, Olefins from conventional and heavy feedstocks: Energy use in steam cracking and alternative processes, Energy 31 (2006) 425-451. doi.org/10.1016/j.energy.2005.04.001.

[13] T. Ren, M.K. Patel, K. Blok, Steam cracking and methane to olefins: Energy use, CO2 emissions and production costs, Energy 33 (2008) 817-833. doi.org/10.1016/j.energy.2008.01.002.

[14] Y.B. Zeldovich, The oxidation of nitrogen in combustion and explosions, J. Acta Physicochimica 21 (1946) 577-628
[15] D.J. Mackinnon, Nitric oxide formation at high temperature, J. Air Pollut. Control Assoc. (1974)
[16] T. Yamamoto, T. Kuwahara, K. Nakaso, T. Yamamoto, Kinetic study of fuel NO formation from pyrrole type nitrogen, Fuel 93 (2012). doi.org/10.1016/j.fuel.2011.09.032.

[17] E.C. Zabetta, M. Hupa, K. Saviharju, Reducing NOx Emissions Using Fuel Staging, Air Staging, and Selective Noncatalytic Reduction in Synergy, Ind. Eng. Chem. Res. 44 (2005) 4552-4561. doi.org/10.1021/ie050051a.

[18] B.Y. Belal, G.S. Li, Z.H. Zhang, H.M. El-Batsh, H.A. Moneib, A.M.A. Attia, The effect of swirl burner design configuration on combustion and emission characteristics of lean pre-vaporized premixed flames, Energy 228 (2021). doi.org/10.1016/j.energy.2021.120622.

[19] C. Herce, A. González-Espinosa, A. Gil, C. Cortés, J. González-Rebordinos, T. Guégués, M. Gil, L. Ferré, F. Brunet, A. Arias, Combustion monitoring in an industrial cracking furnace based on combined CFD and optical techniques, Fuel 280 (2020) 118502. doi.org/10.1016/j.fuel.2020.118502.

[20] D.J. Van Cauwenberge, C.M. Schietekat, J. Floré, K.M. Van Geem, G.B. Marin, CFD-based design of 3D pyrolysis reactors: RANS vs. LES, Chem. Eng. J. 282 (2015) 66-76. doi.org/10.1016/j.cej.2015.03.020.

[21] S. Vangaever, P.A. Reyniers, S.H. Symoens, N.D. Ristic, M.R. Djokic, G.B. Marin, K.M. Van Geem, Pyrometer-based control of a steam cracking furnace, Chem. Eng. Res. Des. 153 (2020) 380-390. doi.org/10.1016/j.cherd.2019.10.023.

[22] F. Wéry, M. Geerts, L.A. Vandewalle, P.A. Reyniers, G.J. Heynderickx, G.B. Marin, K.M. Van Geem, Assessing the CO2 emission reduction potential of steam cracking furnace innovations via computational fluid dynamics: From high-emissivity coatings, over coil modifications to firing control, Chem. Eng. Res. Des. 190 (2023) 129-142. doi.org/10.1016/j.cherd.2022.12.017.

[23] M. Rezaeimanesh, S.A.A. Ghoreyshi, S.M. Peyghambarzadeh, S.H. Hashemabadi, Coke deposition and run length in industrial naphtha thermal cracking furnaces via a quasi-steady state coupled CFD model, Can. J. Chem. Eng. n/a (2022). doi.org/10.1002/cjce.24741.

[24] M.W.M. van Goethem, E. Jelsma, Numerical and experimental study of enhanced heat transfer and pressure drop for high temperature applications, Chem. Eng. Res. Des. 92 (2014) 663-671. doi.org/10.1016/j.cherd.2014.02.009.

[25] J.N. Dedeyne, D.J. Van Cauwenberge, P.A. Reyniers, K.M. Van Geem, G.B. Marin, Large eddy simulation of tubular reactors with spherical dimples, Chem. Eng. J. 380 (2020) 122463. doi.org/10.1016/j.cej.2019.122463.

[26] C.M. Schietekat, M.W.M. van Goethem, K.M. Van Geem, G.B. Marin, Swirl flow tube reactor technology: An experimental and computational fluid dynamics study, Chem. Eng. J. 238 (2014) 56-65. doi.org/10.1016/j.cej.2013.08.086.

[27] L.A. Vandewalle, D.J. Van Cauwenberge, J.N. Dedeyne, K.M. Van Geem, G.B. Marin, Dynamic simulation of fouling in steam cracking reactors using CFD, Chem. Eng. J. 329 (2017) 77-87. doi.org/10.1016/j.cej.2017.06.113.

[28] S. Vangaever, J. Van Thielen, J. Hood, J. Olver, P. Honnerovà, G.J. Heynderickx, K.M. Van Geem, The Effect of Refractory Wall Emissivity on the Energy Efficiency of a Gas-Fired Steam Cracking Pilot Unit, Materials 14 (2021). doi.org/10.3390/ma14040880.

[29] S. Vangaever, P.A. Reyniers, C. Visser, D. Jakobi, G.J. Heynderickx, G.B. Marin, K.M. Van Geem, Computational Fluid Dynamics-Based Study of a High Emissivity Coil Coating in an Industrial Steam Cracker, Ind. Eng. Chem. Res. 57 (2018) 16782-16794. doi.org/10.1021/acs.iecr.8b04068.

[30] J. González Rebordinos, C. Herce, A. González-Espinosa, M. Gil, C. Cortés, F. Brunet, L. Ferré, A. Arias, Evaluation of retrofitting of an industrial steam cracking furnace by means of CFD simulations, Appl. Therm. Eng. 162 (2019) 114206. doi.org/10.1016/j.applthermaleng.2019.114206.

[31] M. Rezaeimanesh, A. Asghar Ghoreyshi, S.M. Peyghambarzadeh, S. Hassan Hashemabadi, A coupled CFD simulation approach for investigating the pyrolysis process in industrial naphtha thermal cracking furnaces, Chin. J. Chem. Eng. 44 (2022) 528-542. doi.org/10.1016/j.cjche.2021.03.028.

[32] V. Yakhot, S.A. Orszag, S. Thangam, T.B. Gatski, C.G. Speziale, Development of turbulence models for shear flows by a double expansion technique, Phys. Fluids A 4 (1992) 1510-1520. doi.org/10.1063/1.858424.

[33] D.M.G. Gregory P. Smith, Michael Frenklach, Nigel W. Moriarty, Boris Eiteneer, Mikhail Goldenberg, C. Thomas Bowman, Ronald K. Hanson, Soonho Song, William C. Gardiner, Jr., Vitali V. Lissianski, and Zhiwei Qin, http://www.me.berkeley.edu/gri_mech/

[34] B. Mayr, R. Prieler, M. Demuth, C. Hochenauer, The usability and limits of the steady flamelet approach in oxy-fuel combustions, Energy 90 (2015) 1478-1489. doi.org/10.1016/j.energy.2015.06.103.

[35] K. Bray, Laminar Flamelets in Turbulent Combustion Modeling, Combust. Sci. Technol. 188 (2016) 1372-1375. 10.1080/00102202.2016.1195819.

[36] H. Pitsch, H. Barths, N. Peters, Three-Dimensional Modeling of NOx and Soot Formation in DI-Diesel Engines Using Detailed Chemistry Based on the Interactive Flamelet Approach, SAE International, 1996.

[37] H. Pitsch, N. Peters, A Consistent Flamelet Formulation for Non-Premixed Combustion Considering Differential Diffusion Effects, Combust. Flame 114 (1998) 26-40. doi.org/10.1016/S0010-2180(97)00278-2.

[38] W.P. Jones, J.H. Whitelaw, Calculation methods for reacting turbulent flows: A review, Combust. Flame 48 (1982) 1-26. doi.org/10.1016/0010-2180(82)90112-2.

[39] B. Marracino, D. Lentini, Radiation Modelling in Non-Luminous Nonpremixed Turbulent Flames, Combust. Sci. Technol. 128 (1997) 23-48. doi.org/10.1080/00102209708935703.

[40] S.R. Mathur, J.Y. Murthy, Coupled Ordinates Method for Multigrid Acceleration of Radiation Calculations, J. Thermophys Heat Transfer 13 (1999) 467-473. doi.org/10.2514/2.6485.

[41] G.D. Raithby, E.H. Chui, A Finite-Volume Method for Predicting a Radiant Heat Transfer in Enclosures With Participating Media, J. Heat Transfer 112 (1990) 415-423. doi.org/10.1115/1.2910394.

[42] T.F. Smith, Z.F. Shen, J.N. Friedman, Evaluation of Coefficients for the Weighted Sum of Gray Gases Model, J. Heat Transfer 104 (1982) 602-608. doi.org/10.1115/1.3245174.

[43] K.M. Van Geem, D. Hudebine, M.F. Reyniers, F. Wahl, J.J. Verstraete, G.B. Marin, Molecular reconstruction of naphtha steam cracking feedstocks based on commercial indices, Comput. Chem. Eng. 31 (2007) 1020-1034. doi.org/10.1016/j.compchemeng.2006.09.001.

[44] K.M. Van Geem, G.J. Heynderickx, G.B. Marin, Effect of radial temperature profiles on yields in steam cracking, AIChE Journal 50 (2004) 173-183. doi.org/10.1002/aic.10016.

[45] K.M. Van Geem, M.F. Reyniers, G.B. Marin, Challenges of Modeling Steam Cracking of Heavy Feedstocks, Oil Gas Sci. Technol. 63 (2008) 79-94. doi.org/10.2516/ogst:2007084.

[46] M.K. Sabbe, K.M. Van Geem, M.-F. Reyniers, G.B. Marin, First principle-based simulation of ethane steam cracking, AIChE Journal 57 (2011) 482-496. doi.org/10.1002/aic.12269.

[47] M. Saeys, M.-F. Reyniers, G.B. Marin, V. Van Speybroeck, M. Waroquier, Ab initio group contribution method for activation energies for radical additions, AIChE Journal 50 (2004) 426-444. doi.org/10.1002/aic.10038.

[48] G.C. Reyniers, G.F. Froment, F.-D. Kopinke, G. Zimmermann, Coke Formation in the Thermal Cracking of Hydrocarbons. 4. Modeling of Coke Formation in Naphtha Cracking, Ind. Eng. Chem. Res. 33 (1994) 2584-2590. doi.org/10.1021/ie00035a009.

[49] P.M. Plehiers, G.C. Reyniers, G.F. Froment, Simulation of the run length of an ethane cracking furnace, Ind. Eng. Chem. Res. 29 (1990) 636-641. doi.org/10.1021/ie00100a022.

[50] S. So, N. Jeong, A. Song, J. Hwang, D. Kim, C. Lee, Measurement of Temperature and H2O Concentration in Premixed CH4/Air Flame Using Two Partially Overlapped H2O Absorption Signals in the Near Infrared Region, Appl. Sci. 11 (2021). doi.org/10.3390/app11083701.

[51] O. Colin, J.-B. Michel, A Two-Dimensional Tabulated Flamelet Combustion Model for Furnace Applications, Flow Turbul. Combust. 97 (2016) 631-662. doi.org/10.1007/s10494-015-9699-9.